









Publication Year	2023
Acceptance in OA	2025-02-04T11:17:26Z
Title	Nature of continuum emission in the source of the water maser super-flare G25.65+1.04
Authors	Bayandina, O. S., Burns, R. A., Kurtz, S. E., MOSCADELLI, Luca, Sobolev, A. M., Stecklum, B., Val'Tts, I. E.
Publisher's version (DOI)	10.1051/0004-6361/202346023
Handle	http://hdl.handle.net/20.500.12386/35797
Journal	ASTRONOMY & ASTROPHYSICS
Volume	673

Nature of continuum emission in the source of the water maser super-flare G25.65+1.04[★]

O. S. Bayandina¹, R. A. Burns^{2,3}, S. E. Kurtz⁴, L. Moscadelli¹, A. M. Sobolev⁵,
B. Stecklum⁶, and I. E. Val'tts⁷

¹ INAF – Osservatorio Astrofisico di Arcetri, Largo E. Fermi 5, 50125 Firenze, Italy
e-mail: olga.bayandina@inaf.it

² National Astronomical Observatory of Japan, 2-21-1 Osawa, Mitaka-shi, Tokyo 181-8588, Japan

³ Korea Astronomy and Space Science Institute, 776 Daedeokdaero, Yuseong, Daejeon 34055, Republic of Korea

⁴ Instituto de Radioastronomía y Astrofísica, Universidad Nacional Autónoma de México, Antig. Carr. a Patzcuaro 8701, Morelia 58089, Mexico

⁵ Ural Federal University, 51 Lenin Str., 620051 Ekaterinburg, Russia

⁶ Thüringer Landessternwarte, Sternwarte 5, 07778 Tautenburg, Germany

⁷ Astro Space Center, P.N. Lebedev Physical Institute of RAS, 84/32 Profsoyuznaya st., Moscow 117997, Russia

Received 30 January 2023 / Accepted 9 March 2023

ABSTRACT

Context. The G25.65+1.04 source is one of the few known ‘super-flare’ water masers in the Milky Way, but in contrast to other super-flare sources, it remains the least studied. In fact, even the nature of the source driving the water maser is still unclear.

Aims. With this project, we aim to clarify the composition and properties of the G25.65+1.04 region by means of examining the parameters of the continuum sources and establishing their association with masers of different types.

Methods. Our previous VLA (*Karl G. Jansky* Very Large Array) observation detected four continuum peaks (VLA 1-4), three of which (VLA 1-3) were closely spaced and presented a linear orientation. However, the observation, which used the VLA B configuration, lacked the spatial resolution to resolve individual sources. A higher-resolution (A configuration) VLA observation of the continuum and spectral lines was conducted in 2019 using the *L*, *S*, *C*, and *Ku* bands.

Results. For the first time, the continuum source VLA 1 – associated with the flaring water maser – is resolved into two components: VLA 1A and 1B. The component VLA 1A and the water maser are found to spatially coincide and are thought to be powered by the same source, a protostar at an early stage of evolution showing active ejection. We argue that VLA 2 pinpoints an actively ejecting high-mass protostar, as it is associated with a 6.7 GHz methanol maser and a magnetised jet traced by a 22 GHz H₂O maser. Highly polarised OH maser emission is detected in the vicinity of VLA 1-2, with the brightest OH maser found in VLA 2. The magnetic field, identified from the OH maser emission, ranges from $\sim +0.4$ mG in VLA 1A to ~ -8 mG in VLA 2.

Conclusions. The G25.65+1.04 region is found to consist of at least two young stellar objects: VLA 1A and VLA 2. Both sources are found to be at an active accretion and ejection stage of evolution.

Key words. stars: formation – masers – stars: individual: G25.65+1.04

1. Introduction

Cosmic masers are one of the key tracers of massive star formation. Masers not only trace morphological elements and kinematics of protostellar systems (e.g., [Moscadelli et al. 2020](#)) but also provide information about the system’s evolutionary status ([Ellingsen et al. 2007](#)) and the physical parameters of the environment (e.g., [Cragg et al. 2005](#)). Moreover, all this is while the maser emission is able to escape dense protostellar shells (a feat beyond the reach of a young protostar itself), and masers are compact and bright enough for interferometric studies (up to space-ground baselines, e.g., [Sobolev et al. 2018](#)).

A particular phenomenon that reveals a detailed picture of a star formation region and the nature of masers themselves is a ‘maser flare’. During such an event, the maser flux density increases significantly compared to its stable state (e.g., [Liljeström & Gwinn 2000](#); [Hirota et al. 2014](#); [Sugiyama et al.](#)

[2019](#); [Colom et al. 2021](#) and works of the Maser Monitoring Organisation (M2O¹)) and traces a variety of phenomena related to the star formation process.

Maser flares vary in brightness and duration and are associated with different types of masers, depending on the nature of the flaring mechanism. For example, the rarest but most outstanding in the sense of providing information on star formation mechanisms are maser flares associated with accretion bursts in massive stars (e.g., [Caratti o Garatti et al. 2017](#); [Hunter et al. 2017](#); [Burns et al. 2020b](#)). During an accretion burst, the luminosity of the central protostar increases, perturbing the entire surrounding region. In the process, different maser species brighten, and new, previously undetected masers are excited (e.g., [Breen et al. 2019](#); [Brogan et al. 2019](#); [MacLeod et al. 2019](#)).

Surprisingly, flares caused by such ‘global’ events are not the brightest. On the contrary, much brighter flares can be

[★] Full Tables 4 and 5 are only available at the CDS via anonymous ftp to cdsarc.cds.unistra.fr (130.79.128.5) or via <https://cdsarc.cds.unistra.fr/viz-bin/cat/J/A+A/673/A60>

¹ A global co-operative of maser monitoring programmes, <https://masermonitoring.org>

caused by a localised and compact phenomenon: overlapping of maser cloudlets along the line of sight of the observer. This type of maser flare is thought to be exclusively associated with water masers. Notably, the flux density of the flare can reach 10^4 – 10^5 Jy, with Orion KL being the prototypical example (Shimoikura et al. 2005; Hirota et al. 2011). This ‘eclipse’ of clouds does not obscure the maser emission but instead amplifies it like a magnifying glass, thanks to the increase in the maser path length along the line of sight to the observer (Deguchi & Watson 1989).

For many years Orion KL was the only known case, but recently the M2O has found at least three more (G25.65+0.05 (Bayandina et al. 2019; Burns et al. 2020a), G34.196–0.592, and G81.174–00.100 (M2O publications, in prep.), suggesting that this type of local maser flare is more common than originally thought. However, the sample is still small, and it is not clear if there is anything special (i.e. rare) about the host sources or if the small number of detections results from a lack of observational effort.

One of the maser super-flares², G25.65+0.05, stands out because it showed multiple flares of increasing flux density with a decreasing time interval between the flares. In the monitoring of Lekht et al. (2018), three flares were detected in 2002, 2010, and 2016 with flux densities increasing from ~ 3 kJy for the first flare to ~ 46 kJy for the last. But the most powerful flares of water emission were detected in 2017, when the source reached flux densities of ~ 70 kJy (Volvach et al. 2017b,a). The source also showed one of the most short-lived bright flares ever detected. Within half a day the flux density of the source changed from ~ 20 to 76 kJy and then in about two days faded back to ~ 20 kJy (Ashimbaeva et al. 2017).

Notably, the distance to the source is an open issue. No trigonometric parallax observations have been made, and distances estimated by less accurate methods range from 2.7 kpc (Sunada et al. 2007) to 12.5 kpc (Green & McClure-Griffiths 2011). The latter value would make the water maser flare in G25.65+0.05 the brightest ever detected in the Galaxy (BeSSeL Survey³ (Reid et al. 2014)).

The G25.65+0.05 region is not only a host of bright H₂O maser flares but also a valuable example of an active star-forming region that has been extensively reported in the literature. The region is perhaps better known as RAFGL 7009S and as Mol 62. The radio continuum emission of the source has been studied multiple times (e.g., Kurtz et al. 1994; Zavagno et al. 2002; Bayandina et al. 2019), but observations have failed to resolve the individual sources constituting the region. It has been established that G25.65+1.05 harbours several protostars, with at least one of them being at the UCHII stage. The VLA observation of the source conducted in response to the H₂O maser flare of 2017 (B configuration, project code 17B-408) resolved the cm-continuum emission into four partly blended components, indexed as VLA 1-4 (Bayandina et al. 2019). However, the exact morphology of the region and the nature of the individual components are still to be established.

Initially, the water maser super-flare was suspected to be a sign of an accretion burst in the region since it was accompanied by a rise in the brightness of the 6.7 GHz methanol maser (Sugiyama et al. 2017). However, the flux density of the near-infrared emission at the water maser position was discovered to decrease (Sobolev et al. 2017, 2019; Stecklum 2017),

not increase, and the NEOWISE 3.4 and 4.6 μm magnitudes remained constant. Moreover, no apparent change in the spatial distribution of 6.7 GHz methanol masers was found at the post-flare epoch (Bayandina et al. 2019). Neither of these facts support the accretion burst hypothesis.

The source is known to show signs of both infall and outflow. The presence of a 6.7 GHz methanol maser emission and strong ice absorption features was interpreted to be caused by an accretion disc (Zavagno et al. 2002). A bipolar outflow was first detected in the CO (1-0) line by Shepherd & Churchwell (1996). Later works indicated that there is either a single but periodic outflow or multiple outflows from multiple sources (Todd & Ramsay Howat 2006; Sánchez-Monge et al. 2013; Navarete et al. 2015). The systemic velocity of the source is $V_{\text{LSR}} \sim +42.2 \text{ km s}^{-1}$ based on ammonia line emission (Molinari et al. 1996).

The VLA observation of Bayandina et al. (2019) revealed a water maser cluster elongated in the east-west direction in the vicinity of VLA 1. The flaring maser spots were found to be extremely compact and to reside in a crowded maser cluster near the apex of a grouping of blue-shifted masers (Bayandina et al. 2019; Burns et al. 2020b). The lateral ‘V’ shape seen on the VLA spot map gave a key to the maser flare interpretation, according to which the masers trace two linear maser ‘sheets’, and from the viewpoint of the observer, they intersect at a position in the sky-plane corresponding to the position of the flaring maser. However, the central source driving the water maser was not detected.

With this work, we present new, higher-resolution VLA observations of the continuum and maser emission in G25.65+0.05 in an attempt to clarify the protostellar population of the region and the origin of water maser flares.

2. Observations and data reduction

We observed G25.65+1.04 on August 1, 2019, with the *Karl G. Jansky* Very Large Array (VLA) in the A configuration (project 19A-423). The observation took two hours, with ~ 20 min of integration time at each of the four (*L*, *S*, *C*, and *Ku*) bands.

Continuum emission was observed in the *S* band with 64 channels of 2 MHz width, and the *L*, *C*, and *Ku* bands were observed with 128 channels of 1 MHz width. Additionally, OH masers at 1665 and 1667 MHz were observed in the *L* band (1024 channels of 0.244 kHz each), and the class II methanol maser at 6.7 GHz was observed in the *C* band (1024 channels of 0.977 kHz each). The source 3C 286 was observed as the flux, delay, and bandpass calibrator. We used two phase calibrator sources: J1851+0035, in the *S* and *L* bands, and J1832–1035, in the *C* and *Ku* bands. A summary of the observation parameters for the continuum and maser data is presented in Tables 1 and 2.

Data reduction was performed using the Common Astronomy Software Applications⁴ (CASA; CASA Team 2022). For the initial data calibration, we used the VLA CASA Calibration Pipeline. Calibrated data were imaged with the CASA task ‘tclean’. We used natural weighting for continuum imaging and Briggs weighting for maser imaging. Gaussian fitting of the images was performed with the CASA task ‘imfit’. A multi-component Gaussian fit was performed on the continuum images for flux densities above the 3σ level (see Table 1 for the 1σ -levels) to accurately estimate positions and flux densities of individual sources.

² We use the term ‘super-flare’ instead of ‘super-burst’ to avoid confusion with accretion bursts.

³ <http://bessel.vlbi-astrometry.org>

⁴ <http://casa.nrao.edu>

Table 1. Observation parameters: Continuum.

Band	Freq. (GHz)	Synth. Beam (arcsec)	PA (°)	uv -range (k λ)	1σ rms ^(a) (μ Jy beam ⁻¹)
<i>L</i>	1.5	1.45×1.03	-10.1	0.13–244	95
<i>S</i>	3	0.80×0.55	-15.2	0.25–481	15
<i>C</i>	6	0.38×0.27	-20.4	0.5–943	12
<i>Ku</i>	15	0.17×0.12	-25.7	1.3–2068	7

Notes. ^(a)The detection threshold is set at the 3σ level.

A two-dimensional Gaussian brightness distribution was fit to all maser emission peaks with a flux density above 3σ (Table 2). We note that we present results for ‘maser spots’, that is, maser emission detected in a single velocity channel of a data cube. The maser spectra were obtained with the CASA Spectral Profile Tool by integrating over an area encompassing all the maser spots.

3. Results

3.1. Continuum

Continuum emission was detected in all observed frequency bands (*L*, *S*, *C*, *Ku*). The continuum images made using the full UV range at each band are presented in Fig. 1, and the parameters of the detected sources are listed in Table 3. Source names follow the convention of Bayandina et al. (2019).

The continuum emission is unresolved at the *L* band and consists of one ~ 2 mJy peak covering the positions of VLA 1-3 and a fainter blended peak of ~ 0.8 mJy at the position of VLA 4 (Fig. 1a). In the *S*-band image, the position of VLA 4 is easily distinguishable, while VLA 1-3 are still blended, with VLA 1-2 forming a single peak of ~ 2.8 mJy and VLA 3 showing no clear peak (Fig. 1b). In the *C*-band image, VLA 1-2 remain largely unresolved, whereas VLA 3 and 4 show clear peaks of ~ 0.7 and 0.5 mJy, respectively (Fig. 1c). The highest-resolution image (*Ku* band, Fig. 1d) revealed five continuum peaks. In addition to the peaks from VLA 2-4, VLA 1 was resolved into two peaks: VLA 1A (~ 0.6 mJy) and VLA 1B (~ 1 mJy). This is the first credible confirmation of VLA 1A and 1B. Our previous lower-resolution *Q*-band VLA image hinted at the double structure of VLA 1, but the emission was still heavily blended between the two peaks (Bayandina et al. 2019).

When deconvolved from the A-configuration *Ku*-band beam of $\sim 0.15''$, all detected sources appeared to be point-like. However, the integrated flux density of VLA 1B is about three times higher than its peak flux density (Fig. 1d and Table 3), suggesting that it may be slightly extended. To examine the spatial extent of the continuum sources in more detail, we prepared a *Ku*-band image using a round restoring beam of 0.109 arcsec (Fig. 2). In this image, VLA 1A and 1B appeared to be slightly extended, while VLA 2-4 appeared unresolved.

Because the continuum emission of VLA 1 and 2 is blended at almost all observed frequencies, evaluation of spectral indices is not possible for these sources. Only VLA 3 and 4 are clearly distinguishable in more than one frequency band (Fig. 1). To estimate the spectral indices of VLA 3 and 4, we prepared *C*- and *Ku*-band continuum images with a round beam of $0.4''$ for VLA 3. For VLA 4, we used *S*-, *C*-, and *Ku*-band fluxes and a round beam of $0.8''$. In both cases, the beam size was determined by the resolution of the lowest frequency image (*C* band for VLA 3 and *S* band for VLA 4; see Table 1). To ensure a proper compar-

ison of flux densities, these images were prepared with identical UV ranges: 0.5 – 943 k λ for VLA 3 (the longest baseline common to the *C* and *Ku* bands in which VLA 3 is clearly distinguishable from the other continuum peaks) and 0.25 – 481 k λ for VLA 4 (the longest baseline common to the *S*, *C*, and *Ku* bands in which the VLA 4 peak is distinguishable). The resulting normalised flux densities are listed in Table 3. In the previous VLA observation of the source, problems were reported with regard to amplitude calibration due to a flare in the flux calibration source (Bayandina et al. 2019). Thus, the integrated flux densities reported in that paper may be overestimated, and we do not include them in our spectral index calculation. A linear least-squares fit to the data points shown in Fig. 3 gives almost the same spectral index of approximately 0.04 for both VLA 3 and VLA 4.

3.2. Masers

3.2.1. The 6.7 GHz methanol maser

The 6.7 GHz methanol maser emission was detected in the velocity range $V_{\text{LSR}} \sim 38$ – 44 km s⁻¹, with a peak of ~ 120 Jy at $V_{\text{LSR}} = 41.82$ km s⁻¹ (Fig. 4). Gaussian fits of the 6.7 GHz methanol maser data cube are presented in Table 4. The maser spots’ spatial distribution agrees well with that of previous epochs (Hu et al. 2016; Bayandina et al. 2019). Three clearly distinguishable maser groups were found in the vicinity of VLA 2, with each group separated from the continuum emission by ~ 0.2 arcsec. The maser spots with the highest flux densities and broadest velocity range ($V_{\text{LSR}} = 41.5$ – 43.8 km s⁻¹) were found to the north-west of the continuum peak and show a linear extent in the southeast-northwest direction. The maser spots to the south-east of VLA 2 show a narrower velocity range $V_{\text{LSR}} = 40$ – 41 km s⁻¹ and have fluxes of ~ 2 Jy. Within this group, there seems to be some structure, with higher-velocity spots to the south and lower-velocity spots to the north. Finally, the maser spots to the south of VLA 2 have velocities more distant from the systemic velocity of the source (42.4 km s⁻¹). This group shows the smallest range of velocities ($V_{\text{LSR}} = 38.3$ – 38.9 km s⁻¹) and the lowest flux densities (~ 1.5 Jy). Following Bayandina et al. (2019), we designated the three spatial groups of the maser spots as ‘S’ for the southern group of the maser spots with $V_{\text{LSR}} \sim 38$ – 39 km s⁻¹, ‘NE’ for the northeastern group with $V_{\text{LSR}} \sim 40$ – 41 km s⁻¹, and ‘NW’ for the northwestern group with $V_{\text{LSR}} \sim 41$ – 44 km s⁻¹ (see Table 4 and Fig. 4).

3.2.2. The 1665 MHz and 1667 MHz OH masers

The OH maser emission was detected in the velocity range $V_{\text{LSR}} = \sim 36$ – 46 km s⁻¹ at 1665 MHz and $V_{\text{LSR}} = \sim 36$ – 42 km s⁻¹ at 1667 MHz (Fig. 5). Both 1665 and 1667 MHz masers show complex, multi-component spectra. The flux density of the 1665 MHz maser reaches ~ 14 Jy ($V_{\text{LSR}} = 41.6$ km s⁻¹), while the strongest 1667 MHz maser is only ~ 0.5 Jy, without a clearly dominant component. The OH emission was detected over a region of ~ 1.4 arcsec in diameter. The 1667 MHz masers extend over a slightly wider area than the 1665 MHz masers, but this may be a consequence of the larger fitting errors of the low-flux 1667 MHz maser spots (Table 5).

Polarisation of OH masers can provide information on magnetic field strength, so we analysed the right (RCP) and left circular polarisation (LCP) data separately. The parameters were obtained for the 1665 and 1667 MHz OH maser data fits are presented in Table 5.

Table 2. Observation parameters: Spectral line.

Maser	Freq.	Synth. Beam (arcsec)	PA ($^{\circ}$)	Spec. res. (km s^{-1})	1σ rms (mJy beam^{-1})
CH ₃ OH	6.7 GHz	0.35×0.26	-11.91	0.04	10
OH	1665 MHz	1.34×1.09	-1.84	0.04	50
OH	1667 MHz	1.34×1.08	-2.61	0.04	50

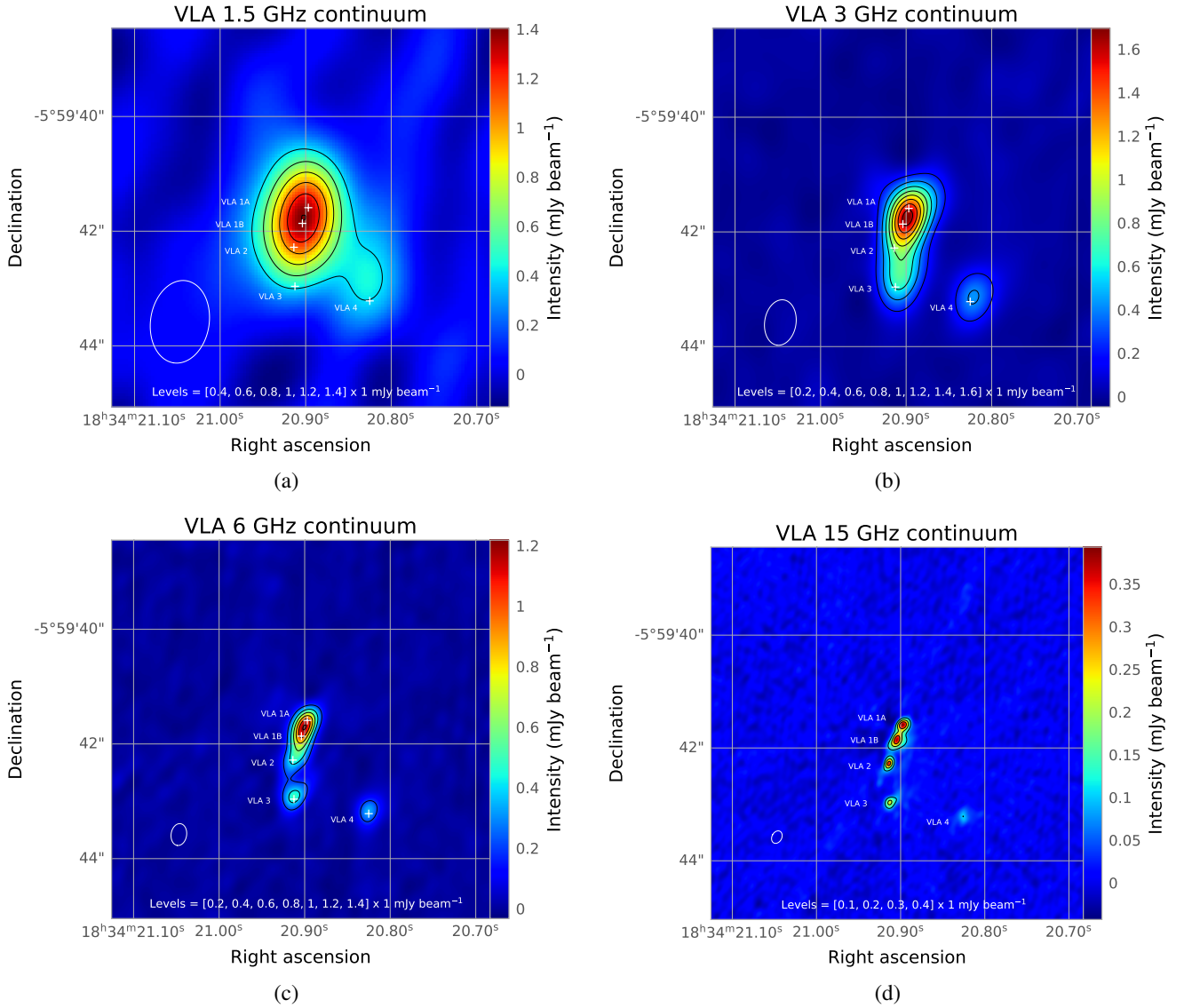


Fig. 1. VLA continuum images of G25.65+1.04 at 1.5, 3, 6, and 15 GHz. The contour levels are indicated in each panel. White crosses and labels mark the detected *Ku*-band continuum peaks from Table 3. The VLA synthesised beam size of each image is shown by the white ellipses in the lower-left corner of the panels. We note that the full UV range was used at each band.

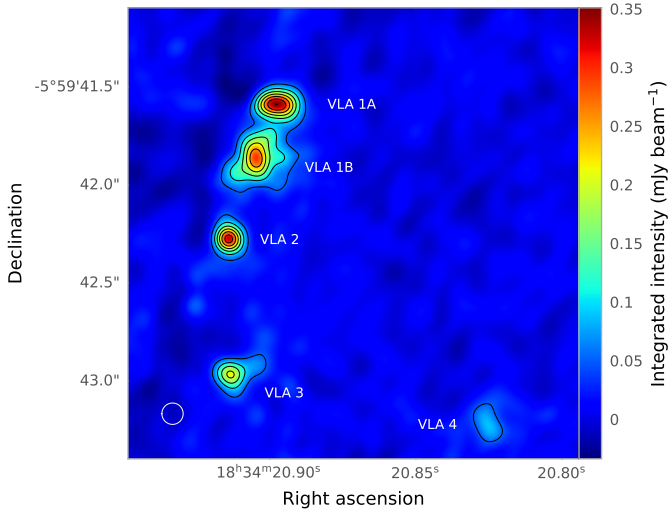
The brightest spectral feature at 1665 MHz ($V_{\text{LSR}} = 41.6 \text{ km s}^{-1}$) shows strong (86%) LCP. In contrast, the other strong lines in the spectrum, which are at $V_{\text{LSR}} = 37.1, 43.1$ and 45.5 km s^{-1} , are almost 100% right polarised. The 1665 MHz masers show a velocity gradient, as maser spots with blue-shifted velocities are found to the south, while spots with red-shifted velocities are to the north. The 1665 maser spots fall into four spatial groups, each one with a different velocity range. The brightest and the most polarised 1665 MHz maser

features (RCP at $V_{\text{LSR}} = 41.6 \text{ km s}^{-1}$ and LCP at $V_{\text{LSR}} = 37.7 \text{ km s}^{-1}$) arise in the same region ~ 0.2 arcsec to the south of VLA 2 (see Fig. 5). The south-west cluster, with velocities $V_{\text{LSR}} \sim 40 \text{ km s}^{-1}$, shows about equal RCP and LCP fluxes. To the north are two maser groups: $V_{\text{LSR}} \sim 43$ (to the east) and $\sim 45 \text{ km s}^{-1}$ (to the west). The eastern clump is more compact and consists of RCP spots only, while the western group is more extended and hosts RCP and LCP spots of almost equal intensity.

Table 3. Parameters of the detected continuum peaks.

Band	Source	RA(J2000) (^h ^m ^s)	Dec(J2000) ([°] ['] ^{''})	Int. flux ^(a) (mJy)	Peak flux ^(a) (mJy beam ⁻¹)	Int. flux _n ^(b) (mJy)
<i>L</i>	VLA 1-3	18:34:20.903±0.002	-05:59:41.77±0.08	1.98±0.26	1.40±0.12	–
	VLA 4	18:34:20.834±0.002	-05:59:42.69±0.06	0.75±0.08	0.48±0.03	–
<i>S</i>	VLA 1-2	18:34:20.899±0.001	-05:59:41.81±0.03	2.80±0.18	1.58±0.07	–
	VLA 3	18:34:20.907±0.0001	-05:59:42.79±0.001	0.82±0.04	0.69±0.02	–
	VLA 4	18:34:20.821±0.0001	-05:59:43.13±0.002	0.47±0.03	0.43±0.02	0.50±0.05 ^(*)
<i>C</i>	VLA 1	18:34:20.901±0.001	-05:59:41.74±0.02	2.48±0.17	1.19±0.06	–
	VLA 2	18:34:20.909±0.0003	-05:59:42.21±0.01	0.93±0.03	0.46±0.01	–
	VLA 3	18:34:20.912±0.0002	-05:59:42.91±0.004	0.69±0.02	0.48±0.01	1.09±0.10 ^(**)
	VLA 4	18:34:20.825±0.0003	-05:59:43.17±0.01	0.47±0.02	0.33±0.01	0.57±0.04 ^(*)
<i>Ku</i>	VLA 1A	18:34:20.897±0.0003	-05:59:41.59±0.004	0.58±0.04	0.39±0.02	–
	VLA 1B	18:34:20.904±0.0004	-05:59:41.86±0.01	0.96±0.07	0.34±0.02	–
	VLA 2	18:34:20.914±0.0002	-05:59:42.28±0.01	0.46±0.04	0.32±0.02	–
	VLA 3	18:34:20.913±0.001	-05:59:42.96±0.01	0.41±0.05	0.20±0.02	1.13±0.15 ^(**)
	VLA 4	18:34:20.825±0.002	-05:59:43.22±0.02	0.31±0.08	0.09±0.02	0.53±0.08 ^(**)

Notes. ^(a)The parameters were obtained from the full UV range images presented in Fig. 1. ^(b)The normalised flux densities used for the spectral energy distributions (Fig. 3): ^(*) values obtained for VLA 3 using a round beam and 943 kλ UV range (the longest baseline common to the bands at which VLA 3 is resolved), ^(**) values obtained for VLA 4 using a round beam and 481 kλ UV range (the longest baseline common to the bands at which VLA 4 is resolved).


Fig. 2. VLA *Ku*-band continuum image of G25.65+1.04 deconvolved with a round beam.

Considering the low flux densities of the 1667 MHz spectral features, we can provide only a rough estimate of their polarisation. The 1667 MHz maser feature at $V_{\text{LSR}} \sim 38 \text{ km s}^{-1}$ seems to show strong right circular polarisation, while the feature at $V_{\text{LSR}} \sim 40.5 \text{ km s}^{-1}$ is mostly left polarised. The 1667 MHz masers, although spatially separated in velocity, do not show a uniform trend as the 1665 MHz masers do (see Fig. 5). The northern-most 1667 MHz masers have blue-shifted velocities of $\sim 36 \text{ km s}^{-1}$ and show no significant level of polarisation. We note that no 1665 MHz masers were detected in this northern region. The southern-most group of the OH masers at 1667 MHz with $V_{\text{LSR}} \sim 38 \text{ km s}^{-1}$ shows strong right circular polarisation. And the group between them, with $V_{\text{LSR}} \sim 40\text{--}42 \text{ km s}^{-1}$, is left circularly polarised. Although there are no spectral features detected at the same velocities at both 1665 and 1667 MHz, it is noteworthy that the features with $V_{\text{LSR}} \sim 38 \text{ km s}^{-1}$ show dom-

inant RCP emission at both frequencies, and the features with $V_{\text{LSR}} \sim 42 \text{ km s}^{-1}$ are both LCP.

4. Discussion

4.1. General comments

To provide an overview of the continuum and maser emission in the G25.65+1.04 region, we collected the results obtained in this work and the 22 GHz H₂O maser data from Bayandina et al. (2019) and Burns et al. (2020a) in Fig. 6. The inclusion of the water maser data in the analysis makes it possible to consider maser flares in the context of the region. The water maser data from Burns et al. (2020a) was obtained with the European VLBI Network (EVN) with the synthesised beam 1.2×0.7 mas in October 2017 right after the brightest water maser flare of that year (Volvach et al. 2017a,b), while the data from Bayandina et al. (2019) was obtained with the VLA synthesised beam 0.35×0.25 arcsec in December 2017 (about two months after the flare).

A wider view of the region, including the large-scale outflow (Shepherd & Churchwell 1996; Sánchez-Monge et al. 2013; Todd & Ramsay Howat 2006) and 44 GHz methanol maser data (Bayandina et al. 2019), is shown in Fig. 7. We note that in Fig. 7 we indicate the orientation of the molecular outflows but not their origin or physical extent. Determining the exact source of an outflow was beyond the scope of the works in which these outflows were identified (Shepherd & Churchwell 1996; Todd & Ramsay Howat 2006; Sánchez-Monge et al. 2013). The central source of G25.65+1.04 was assumed to be the single UCHII region reported in Kurtz et al. (1994). According to Shepherd & Churchwell (1996), the outflow traced by ¹²CO ($J = 1\text{--}0$) shows a well-defined red lobe to the north-west and a blue lobe to the south-east, with a projected length of $\sim 0.5 \text{ pc}$. The H₂ outflow described in (Todd & Ramsay Howat 2006) shows a similar length of $\sim 70 \text{ arcsec}$ ($\sim 0.7 \text{ pc}$ at 2.08 pc) and a northeast-southwest orientation between the largest H₂ knots (Fig. 7). However, the latest molecular line study of the region revealed almost north-south SiO (2–1), SiO (5–4), and HCO⁺

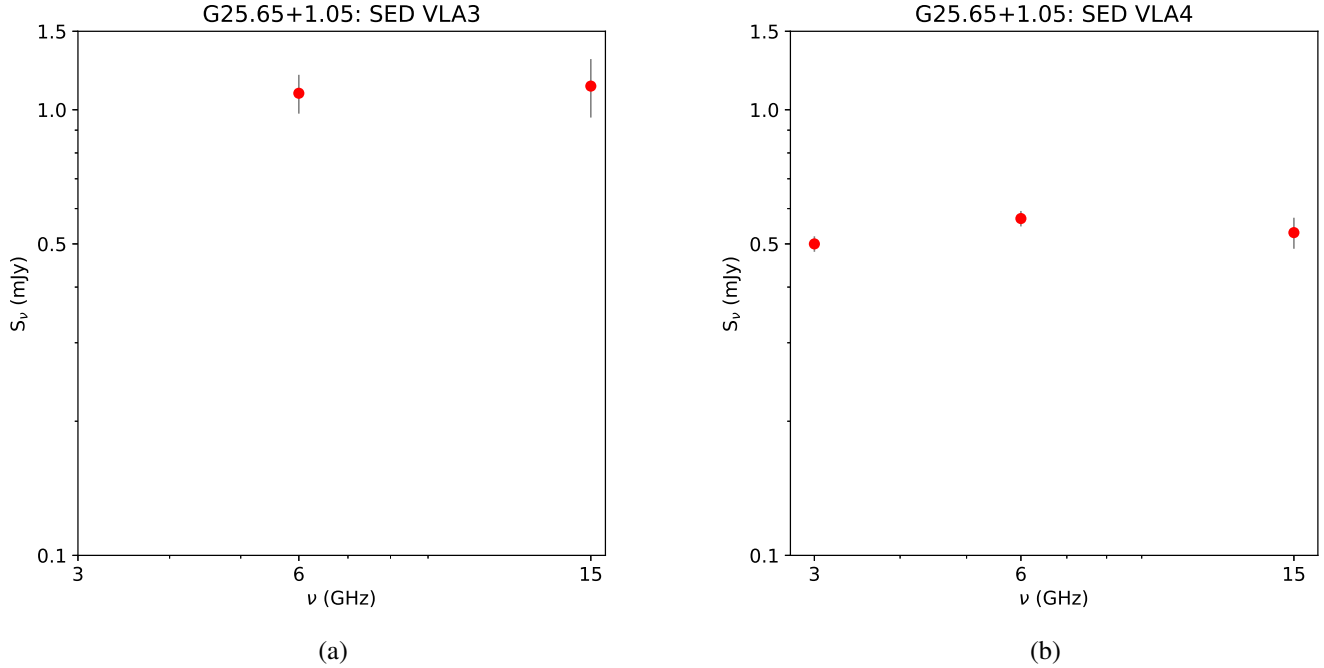


Fig. 3. Spectral energy distribution for the continuum sources (a) VLA 3 and (b) VLA 4. The filled circles represent the normalised integrated flux densities with error bars (see Table 3). The presented flux density values were obtained using round beams and UV ranges of 0–943 $k\lambda$ for VLA 3 and of 0–481 $k\lambda$ for VLA 4 (for details see the text of Sect. 3.1).

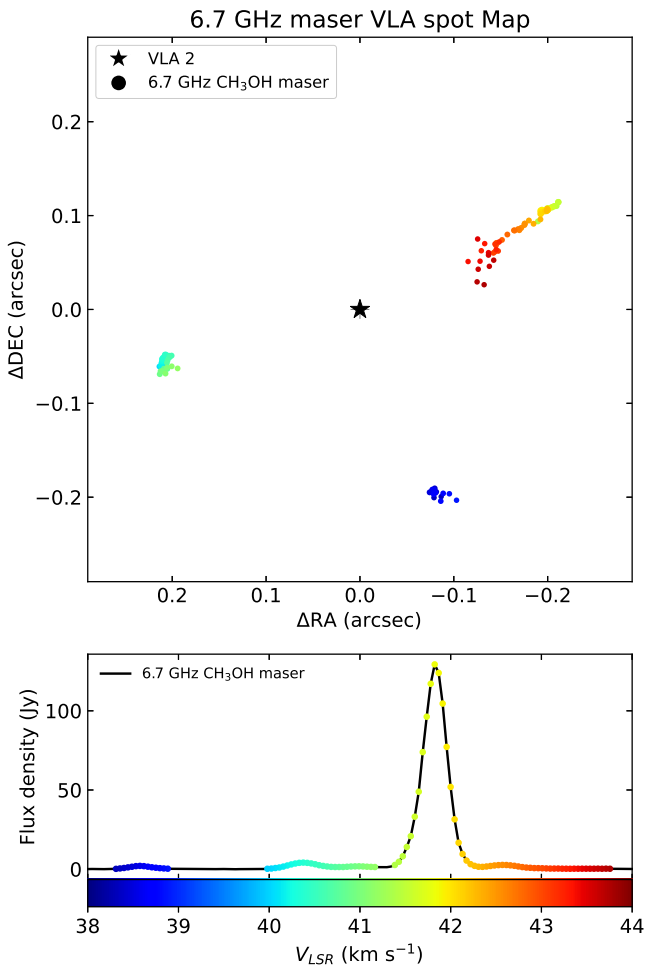


Fig. 4. VLA spot map of the 6.7 GHz maser. The spot map is centred on the position of VLA 2 (see Table 3).

(1–0) outflows of about 0.7 pc size using a 3.1 kpc distance to the source (Sánchez-Monge et al. 2013). It is unclear whether the listed outflow tracers track different outflows or different spatial parts and/or evolutionary stages of the same large-scale outflow. Nonetheless, we note that SiO emission is known to be a reliable jet tracer (e.g., Guillet et al. 2009), while CO and HCO mark the low-velocity extended component of outflow (e.g., Cesaroni et al. 1999).

Additionally, we used our OH data to examine magnetic fields associated with the centimetre continuum peaks. The large VLA beam at the L and, in conjunction with the moderate flux density of the OH maser emission, leads to relatively large positional uncertainties that prohibit a robust identification of Zeeman pairs. Thus, we consider our OH-Zeeman analysis to provide only a rough estimate of the magnetic field strength. We searched the OH data (Table 5) for spatially coincident RCP and LCP maser spots, which are indicative of Zeeman pairs. The maser spots were considered to be a Zeeman pair if their positions matched within the average positional uncertainty of the data (~ 0.05 arcsec; see Table 5). The strength of the corresponding magnetic field was calculated assuming the Zeeman splitting coefficients reported by Davies et al. (1974). Because the positional uncertainty of the OH data is relatively large, in the figures below we indicate the average magnetic field strength estimates based on the data of several Zeeman pairs in a particular region. The spectral resolution of the OH data is 0.04 km s^{-1} . Thus, we considered the uncertainty of the magnetic field to be 0.1 mG. Considering all these data, in the next sections we discuss the nature of each centimetre continuum source detected in our VLA observation.

4.2. VLA 1A

Since resolving the continuum emission of G25.65+1.04 into four separate sources (Bayandina et al. 2019), the nature of

Table 4. Parameters of the 6.7 GHz CH₃OH maser.

Group	RA(J2000) (^h ^m ^s)	Dec(J2000) ([°] ['] ^{''})	Integrated flux (mJy)	Peak flux (mJy beam ⁻¹)	V _{LSR} (km s ⁻¹)
S	18:34:20.9080±0.0006	-05:59:42.480±0.010	0.15±0.02	0.16±0.01	38.31
	18:34:20.9085±0.0006	-05:59:42.482±0.009	0.37±0.03	0.29±0.02	38.36
	18:34:20.9084±0.0004	-05:59:42.475±0.007	0.56±0.05	0.51±0.02	38.40

Notes. Table 4 is published in its entirety in machine-readable format at the CDS. A portion is shown here for guidance regarding its form and content.

Table 5. Parameters of the 1665 and 1667 MHz OH masers.

Freq.	Pol.	RA(J2000) (^h ^m ^s)	Dec(J2000) ([°] ['] ^{''})	Integrated flux (mJy)	Peak flux (mJy beam ⁻¹)	V _{LSR} (km s ⁻¹)
1665	R	18:34:20.9151±0.0061	-05:59:42.557±0.076	0.84±0.14	0.47±0.05	36.68
		18:34:20.9234±0.0037	-05:59:42.481±0.052	1.02±0.13	0.69±0.06	36.72
		18:34:20.9234±0.0038	-05:59:42.572±0.049	0.99±0.12	0.66±0.05	36.76

Notes. Table 5 is published in its entirety in machine-readable format at the CDS. A portion is shown here for guidance regarding its form and content.

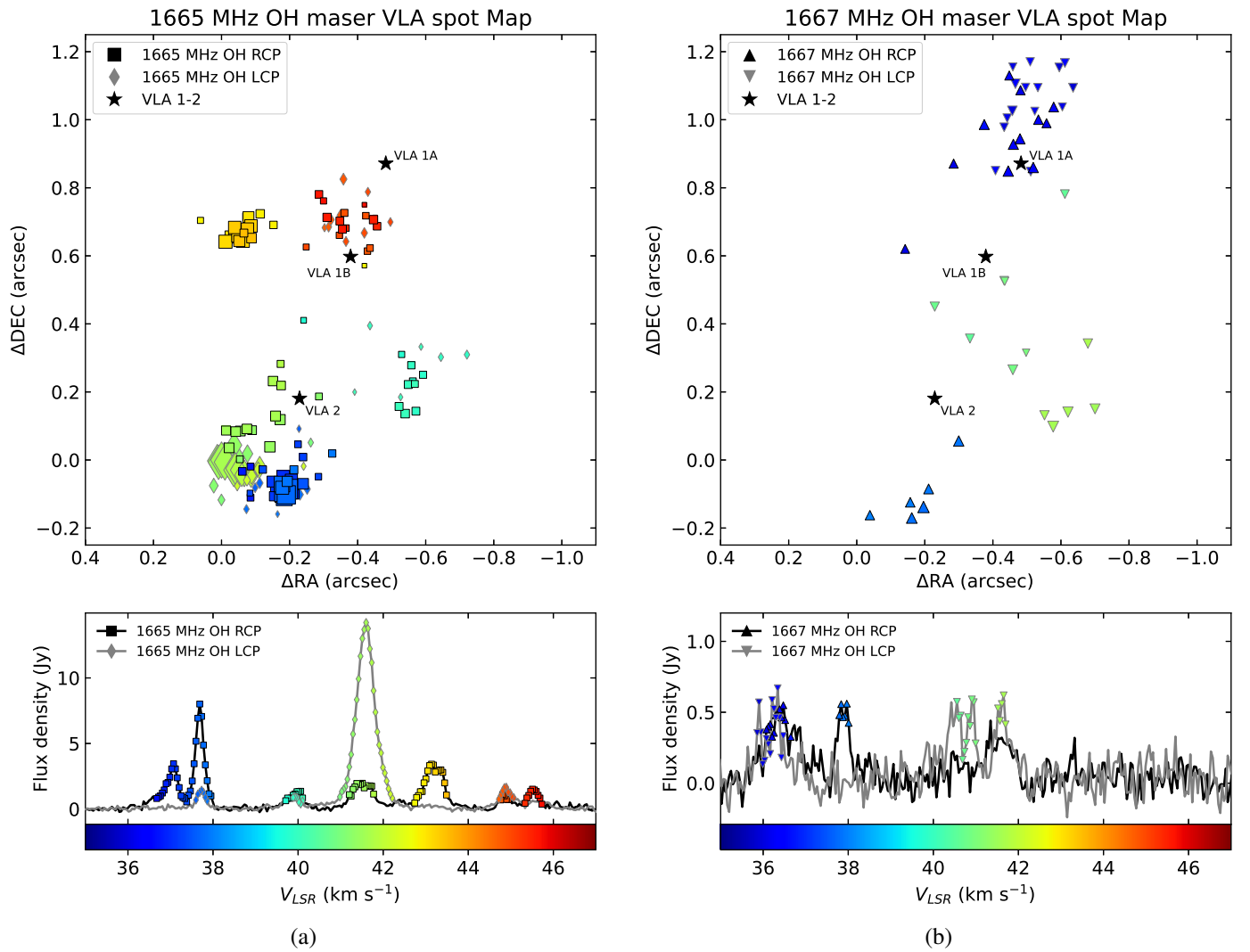


Fig. 5. VLA spot maps of the (a) 1665 MHz and (b) 1667 MHz OH maser. The spot map is centred on the position of the brightest OH(1665) maser (see Table 5).

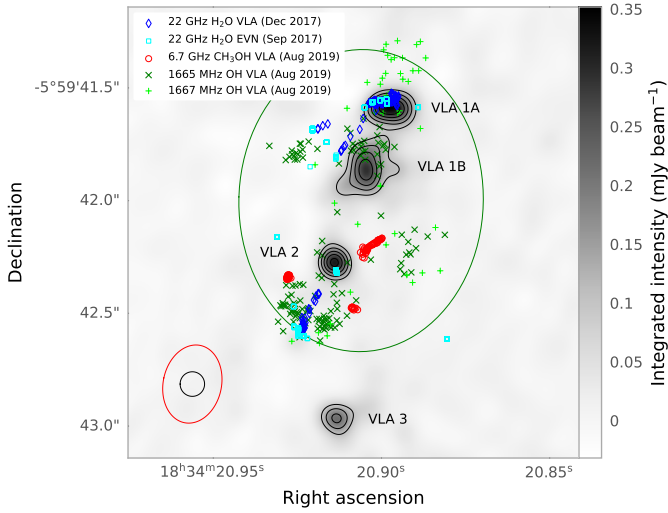


Fig. 6. Centimetre continuum sources and masers detected with the VLA (this paper and Bayandina et al. 2019) and EVN (Burns et al. 2020a) in G25.65+1.04. Black, red, and green ellipses show the VLA synthesised beams of the continuum, the 6.7 GHz methanol maser, and the 1665/1667 MHz OH maser data, respectively. We note that the EVN data from Burns et al. (2020a) was obtained with a synthesised beam of 1.2×0.7 mas.

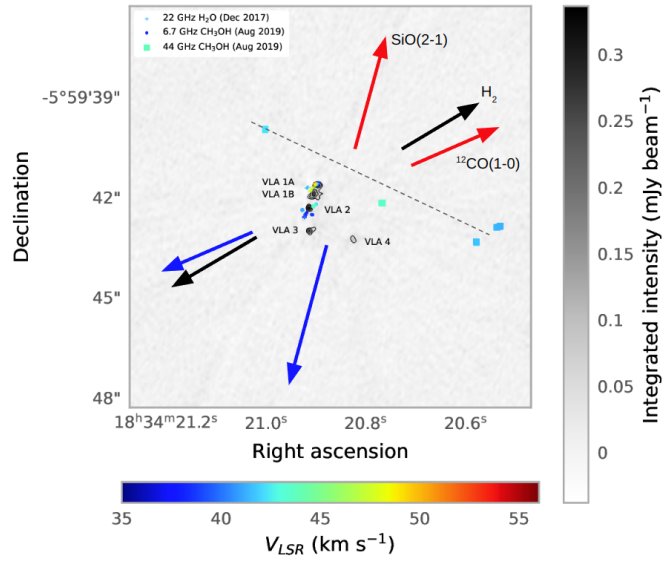
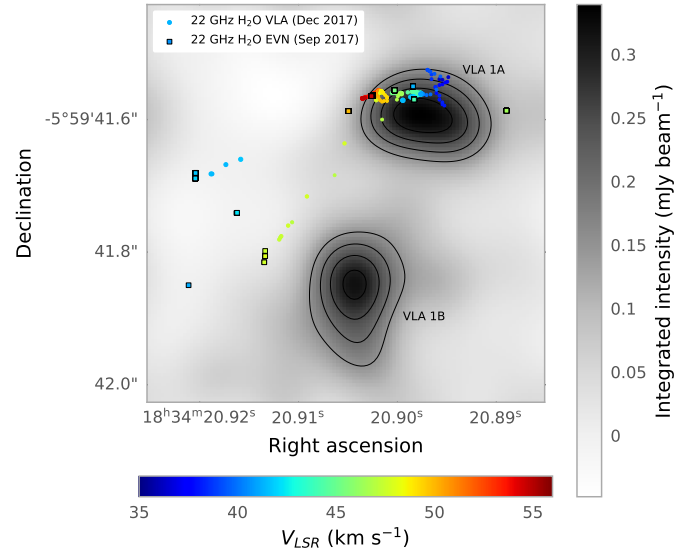


Fig. 8. Zoom in on the H₂O maser activity in the VLA 1 region. Upper panel: H₂O masers detected in the vicinity of VLA 1A and 1B with VLA (Bayandina et al. 2019) and EVN (Burns et al. 2020a). Lower panel: part of the 22 GHz H₂O maser emission detected in the vicinity of VLA 1A with VLA (Bayandina et al. 2019).

Fig. 7. Outflow activity in G25.65+1.04. The ¹²CO data is from Shepherd & Churchwell (1996), SiO(2-1) data is from Sánchez-Monge et al. (2013), and H₂ data is from Todd & Ramsay Howat (2006). Red arrows mark red-shifted outflow lobes, and blue arrows highlight blue-shifted lobes. The arrows indicate the orientation of the outflows but not their extent or origin.

VLA 1 has attracted the most interest because this source is associated with the extraordinary 22 GHz water maser flare of 2017. In the present VLA A configuration observation, for the first time, we reliably resolved VLA 1 into two sources: VLA 1A and VLA 1B.

As the centimetre continuum emission from VLA 1 was resolved in only one band, we cannot confidently estimate the spectral index of the two components and establish their nature solely based on the continuum data. Thus, we review source models based on the additional data we have collected in this study and from the literature.

The most active site of water maser emission in the region is found in the vicinity of VLA 1A (Bayandina et al. 2019; Burns et al. 2020a). The water masers occupy a ~ 0.2 arcsec region and velocity range of $35\text{--}55\text{ km s}^{-1}$ (Fig. 8, upper panel). The brightest H₂O maser emission resides north-east from VLA 1A and shows the same east-west extent as the VLA 1A centimetre continuum data deconvolved with a round beam. Water maser emission is also found between VLA 1A and 1B. The extended part of the water maser emission detected with the VLA (Bayandina et al. 2019) is arranged in two northwest-southeast elongated clusters, with $V_{\text{LSR}} \sim 41.5\text{ km s}^{-1}$ (G1 in Bayandina et al. 2019) and $\sim 47.5\text{ km s}^{-1}$ (G3 in Bayandina et al. 2019), and located to the east of VLA 1A and 1B. The compact emission detected with the EVN (Burns et al. 2020a) marks the base and the ends of these elongated clusters.

Centimetre radio continuum alongside water masers is often associated with jets; thus, the continuum source VLA 1A

may mark a radio jet. The east-west extent of VLA 1A is ~ 0.2 arcsec (Fig. 8, upper panel), while the water maser emission comes from a region almost two times smaller, and it may mark the inner, compact base of a jet (Fig. 8, lower panel). The east-west orientation of this presumed jet coincides with the extent of the 44 GHz methanol maser emission (Bayandina et al. 2019), which is usually associated with large-scale outflows (see Fig. 7a). A few weak H₂ knots are found in the same direction quite close to the centimetre continuum peaks (Todd & Ramsay Howat 2006; Navarete et al. 2015).

The cluster with velocities of ~ 42 – 54 km s⁻¹ (Fig. 8, lower panel) hosting the flaring 22 GHz water maser is elongated in the east-west direction and consists of three spatial structures showing velocity gradients. The maser spots with red-shifted ($V_{\text{LSR}} \sim 51$ km s⁻¹) and blue-shifted ($V_{\text{LSR}} \sim 44$ km s⁻¹) velocities were found to the east and north, respectively, and they form two V-shaped structures. The central part of the emission with $V_{\text{LSR}} \sim 49$ km s⁻¹ shows a round shape and low flux density. The water maser flare of 2017 was found to originate in the western V-shaped region of the cluster (see red cross in the lower panel of Fig. 8) Bayandina et al. (2019), Burns et al. (2020a). Taking into account the V-shape of the blue- and red-shifted clusters as well as their symmetrical orientation relative to one other, the water maser emission may trace jet-driven bow shocks. Assuming the angular separation between the supposed red and blue lobes of ~ 200 AU (~ 0.1 arcsec at ~ 2.08 kpc), the dynamic age of the jet driving them would be ~ 80 yr. Accretion is known to be closely correlated with ejection (e.g., Caratti o Garatti et al. 2015; Cesaroni et al. 2018); thus, the presence of such a young ejection event would indicate that the accretion in VLA 1A is non-steady or episodic.

The possibility that the east-west elongation of the water maser spots with $V_{\text{LSR}} \sim 42$ – 54 km s⁻¹ (Fig. 8) trace an accretion disc around a protostar seems unlikely. Considering the spatial extent of the maser emission in the east-west direction of ~ 200 AU and its velocity range of ~ 12 km s⁻¹ (Fig. 8, lower panel), we estimate the mass of an assumed central source to be $\sim 30 M_{\odot}$.

Notably, only 1667 MHz OH masers were found in the vicinity of VLA 1A, and no OH emission at 1665 MHz was detected. The OH(1667) emission is weak (~ 0.5 Jy), has blue-shifted velocities (~ 36.5 km s⁻¹), and consists of both left- and right-polarised spots. The OH masers at 1667 MHz are known to be the dominant maser in regions of $T_k = 50$ – 75 K and OH densities of 25 – 60 cm⁻³, but importantly, they have smaller velocity shifts over the propagation length than the 1665 MHz OH masers (Gray et al. 1992). Consequently, following Gray et al. (1992), OH masers at 1665 and 1667 MHz arise under similar physical conditions, but OH(1667) forms in the absence of a well-defined velocity gradient. In the case of G25.65+1.04, we can assume that the region to the north-west of VLA 1A is the least affected by the large-scale outflow, and the northern OH masers at 1667 MHz arise in more quiescent gas due to the screen offered by the envelope around VLA 1A. In contrast, the most turbulent region is located to the south of VLA 1A where the flow from VLA 2 impacts with the southern portion of the VLA 1A envelope.

Using the OH data, we evaluated the magnetic field associated with VLA 1A (Fig. 9). Two Zeeman pairs located to the south of the VLA 1A peak position yield about the same value of magnetic field strength: $\sim +0.35$ mG. The results obtained for the remaining pairs identified in the vicinity of VLA 1A are less reliable. The calculated magnetic field changes from $\sim +1.2$ mG to the north-west of VLA 1A to ~ -0.4 mG to the north-east. In

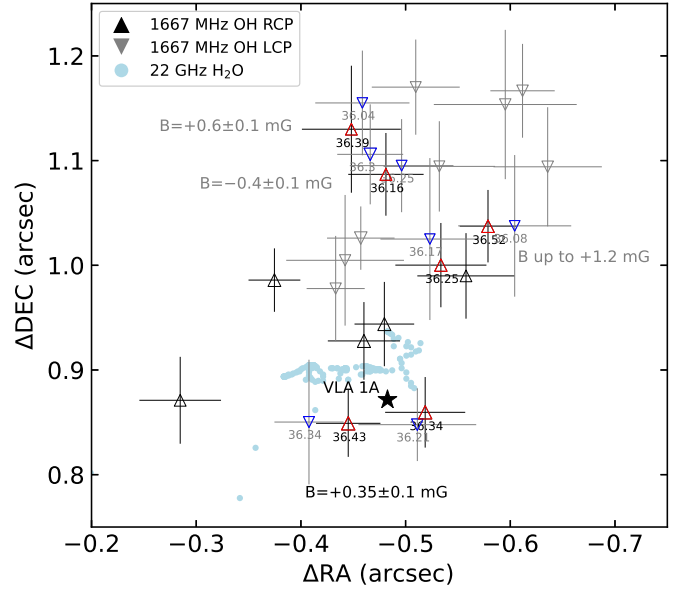


Fig. 9. Possible Zeeman pairs of the 1667 MHz OH masers in the vicinity of VLA 1A. The RCP maser spots of a Zeeman pair are marked with red and LCP pairs are blue. Position errors are marked by crosses (RCP in black; LCP in grey). The average values of the estimated magnetic fields are indicated next to the possible Zeeman pairs. The more robust values, that is, those with close spatial association of a pair and/or multiple pairs that provide the same number, are in black, and less robust values are in grey.

summary, we find that the VLA 1A region shows a weak positive magnetic field.

4.3. VLA 1B

In contrast to VLA 1A, the centimetre continuum of VLA 1B shows a north-south extent (Fig. 2). The elongated and irregular shape of the source suggests a more complex (possibly double) structure that remains unresolved by the VLA beam.

The only maser activity found in the vicinity of VLA 1B is the OH maser emission at 1665 MHz. These maser spots were found to the north of VLA 1B, with a ~ 0.3 arcsec (~ 600 AU) cluster of red-shifted maser spots ($V_{\text{LSR}} \sim 44$ – 46 km s⁻¹; red cluster in Fig. 5a) stretching from VLA 1B to the north and a more compact cluster (~ 0.15 arcsec or ~ 300 AU) of maser spots with $V_{\text{LSR}} \sim 43$ km s⁻¹ (yellow cluster in Fig. 5a) about 0.3 arcsec to the north-east of VLA 1B. The emission of the ‘red’ cluster ($V_{\text{LSR}} \sim 44$ – 46 km s⁻¹; Fig. 5a) overlaps with the centimetre continuum (Fig. 6), has a low flux density (~ 2 Jy), and shows almost equal RCP and LCP fluxes. The ‘yellow’ cluster ($V_{\text{LSR}} \sim 43$ km s⁻¹; Fig. 5a) is approximately two times brighter (~ 4 Jy) and 100% RCP. We note that the apparent compactness of the yellow cluster is at least in part due to its higher flux density. A few weak OH masers at 1667 MHz were found to the south of VLA 1B (Fig. 5b).

The OH(1665) masers in the vicinity of VLA 1B intersect with the G1 and G2 H₂O maser groups of VLA 1A (Fig. 6). The G1 H₂O maser group ($V_{\text{LSR}} \sim 41.5$ km s⁻¹) resides to the north-west from the ‘yellow’ OH group ($V_{\text{LSR}} \sim 43$ km s⁻¹). The string of water maser spots composing G1 connects VLA 1A and the yellow OH group, and it may mark a region of interaction of shock waves with the interstellar medium, while the OH cluster may trace a denser OH-rich region. The G2 H₂O maser group

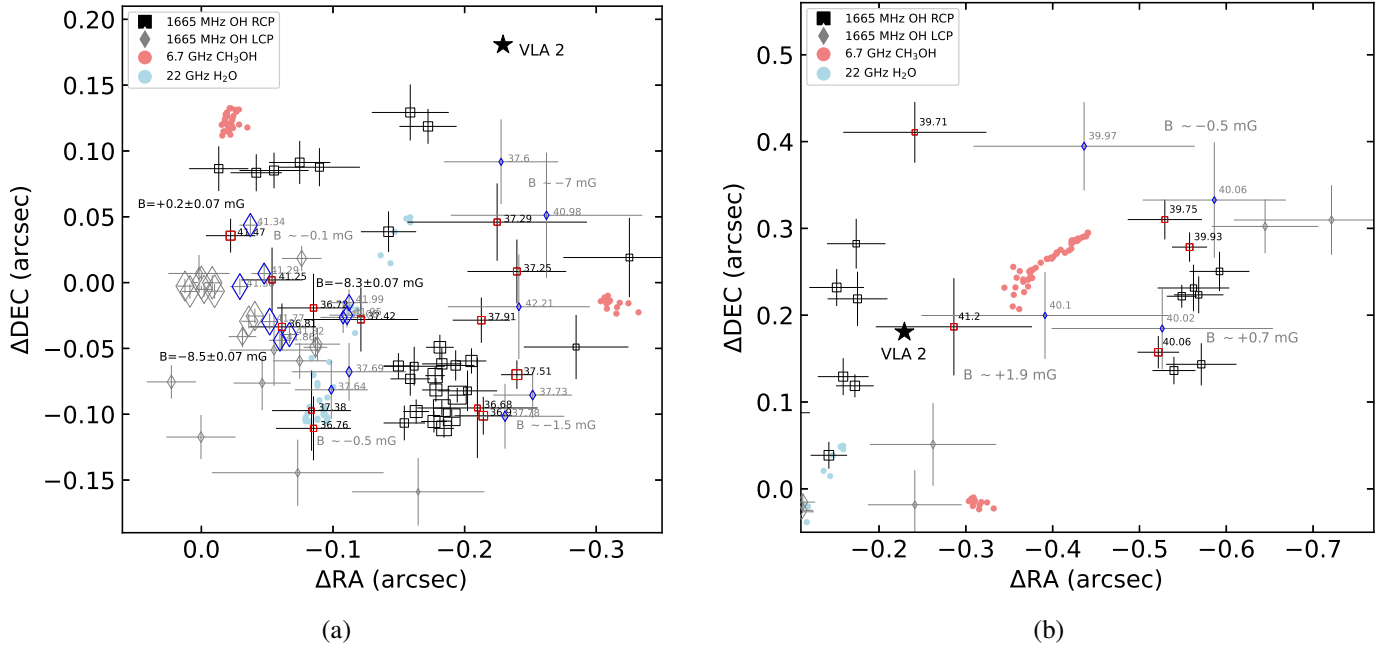


Fig. 11. Possible Zeeman pairs in the 1665 MHz OH maser (a) to the north and (b) to the west of VLA 2. The RCP maser spots of a Zeeman pair are marked red and LCP in blue. Position errors are marked by crosses (RCP in black; LCP in grey). The average values of the estimated magnetic fields are indicated next to the possible Zeeman pairs. More robust values, that is, those with close spatial association of a pair and/or a few pairs that provide the same number, are in black, and less robust values are in grey.

maser spots were detected in the plane of the putative 6.7 GHz methanol maser disc. The Zeeman pairs in the vicinity of the 22 GHz water masers show a magnetic field strength as high as -8.5 ± 0.07 mG. This is the strongest magnetic field found in G25.65+1.04. The eastern OH region consists of a smaller number of maser spots with lower flux densities. Thus, the identified Zeeman pairs are less reliable. The magnetic field here seems to be ~ 0.5 mG, while its orientation is not clear.

Taking into account all of the above, we consider VLA 2 to be a site of high ejection activity. We propose that all 22 GHz water masers, the NE and S methanol maser groups, and the OH masers southeast of VLA 2 (Fig. 6) are associated with the blue lobe of the jet and/or outflow. But the NW methanol maser group is associated with the red lobe. The 22 GHz water masers seem to trace the red lobe of a magnetised jet surrounded by OH masering gas, while the 6.7 GHz masers are associated with the cavity walls. To verify the proposed model, proper motion measurements of the 6.7 GHz methanol masers are required.

4.5. VLA 3

In contrast to the previously described sources, VLA 3 lacks maser emission at any of the observed frequencies. The source is clearly seen at 6 and 15 GHz (Fig. 1) with an integrated flux density of ~ 1 mJy. Based on the two data points we have, the object has a flat spectral index (Fig. 3). We note that in Bayandina et al. (2019), similar values of the integrated flux density of ~ 1 mJy were reported at 22 and 45 GHz.

We highlight that VLA 3 is at the southern end of the line formed by the sources VLA 1-3. If we assume VLA 2 to be the source driving the large-scale outflows, VLA 3 may mark a knot in a jet driving the northwest-southeast large-scale outflow. However, our study does not have any additional evidence suitable for verifying the nature of this source.

4.6. VLA 4

The source VLA 4 is located west of VLA 1-3, making it the only continuum source not aligned with the others. The separation between VLA 4 and the other continuum peaks suggests that it may not have any direct physical association with the latter. Of all the sources in the field, VLA 4 has the weakest integrated flux densities (~ 0.5 mJy). However, the source is detected at all observed frequencies (Fig. 1), and its isolated position allows us to obtain reliable flux densities without the complication of blending.

Similar to VLA 3, VLA 4 has a flat spectral index (Fig. 3). In Bayandina et al. (2019), the source showed a similar flux of ~ 0.5 mJy at 22 GHz but was not detected in the higher-resolution 44 GHz image. The source has a slightly elongated structure in the north-south direction (Fig. 2), but the low signal-to-noise ratio prevents us from drawing any conclusions based on the source morphology.

5. Conclusions

The centimetre continuum in the *L*, *S*, *C*, and *Ku* bands as well as the 6.7 GHz methanol and 1665/1667 MHz OH masers were observed in G25.65+1.04 with the VLA A configuration. We obtained centimetre continuum images of the source with the highest spatial resolution to date. For the first time, centimetre continuum emission of the source VLA 1 has been resolved into two separate sources: VLA 1A and VLA 1B.

Previously, and based on prior VLA observations, the OH masers were thought to be associated with VLA 3. Our new, higher-resolution VLA observations show that the OH emission is found over a larger area, including the positions of VLA 1-2, with the brightest maser spots detected in the vicinity of VLA 2.

In addition, VLA 1A is found to be associated with the 22 GHz water maser that showed super-flares in 2017. Both the centimetre continuum emission and the water masers show the

same east-west elongation. We interpret this elongation of the water masers as a tracer of jet-driven shocks. The dynamic age of the putative jet is estimated to be approximately 80 years. In the vicinity of VLA 1A, an OH maser emission is detected only at 1667 MHz, which indicates the absence of a well-defined velocity gradient (i.e. a lower-velocity environment compared to the OH(1665) regions). Thus, the north-west region from VLA 1A seems to be the least affected by a large-scale outflow from VLA 2 due to the screening provided by VLA 1A's envelope. The magnetic field, identified through the OH maser emission, is positive and has a strength of $\sim+0.4$ mG in the vicinity of the VLA 1A continuum peak and water masers.

Regarding VLA 1B, it is primarily associated with OH masers. This OH maser emission shows both RCP and LCP spots around the continuum peak and a highly right-polarised maser cluster to the east. The estimated magnetic field in VLA 1B is $\sim+1$ mG. Notably, VLA 1B may mark an interaction region between an outflow from VLA 2 and a higher density medium in the vicinity of VLA 1A.

Finally, VLA 2 is associated with 6.7 GHz methanol masers, 22 GHz water masers, and the strongest OH masers. The 6.7 GHz methanol masers are assumed to trace the cavity walls of an outflow driven by VLA 2. The previously reported water masers are interpreted to be associated with a jet surrounded by highly polarised OH emission, which suggests that the jet is magnetised. The magnetic field of ~-8 mG found in the vicinity of the 22 GHz water maser jet in VLA 2 is the strongest in the region.

Acknowledgements. This paper reports data from VLA program 19A-423. The National Radio Astronomy Observatory is a facility of the National Science Foundation operated under cooperative agreement by Associated Universities, Inc. O.B. acknowledges financial support from the Italian Ministry of University and Research - Project Proposal CIR01_00010. The work of AMS was supported by the Ministry of science and higher education of the Russian Federation, agreement FEUZ-2023-0019.

References

- Ashimbaeva, N. T., Platonov, M. A., Rudnitskij, G. M., & Tolmachev, A. M. 2017, *ATel*, 11042, 1
- Bayandina, O. S., Burns, R. A., Kurtz, S. E., Shakhvorostova, N. N., & Val'ts, I. E. 2019, *ApJ*, 884, 140
- Breen, S. L., Sobolev, A. M., Kaczmarek, J. F., et al. 2019, *ApJ*, 876, L25
- Brogan, C. L., Hunter, T. R., Towner, A. P. M., et al. 2019, *ApJ*, 881, L39
- Burns, R. A., Sugiyama, K., Hirota, T., et al. 2020a, *Nat. Astron.*, 4, 506
- Burns, R. A., Orosz, G., Bayandina, O., et al. 2020b, *MNRAS*, 491, 4069
- Caratti o Garatti, A., Stecklum, B., Linz, H., Garcia Lopez, R., & Sanna, A. 2015, *A&A*, 573, A82
- Caratti o Garatti, A., Stecklum, B., & Garcia Lopez, R. 2017, *Nat. Phys.*, 13, 276
- CASA Team (Bean, B., et al.) 2022, *PASP*, 134, 114501
- Cesaroni, R., Felli, M., Jenness, T., et al. 1999, *A&A*, 345, 949
- Cesaroni, R., Moscadelli, L., Neri, R., et al. 2018, *A&A*, 612, A103
- Colom, P., Ashimbaeva, N. T., Lekht, E. E., et al. 2021, *MNRAS*, 507, 3285
- Cragg, D. M., Sobolev, A. M., & Godfrey, P. D. 2005, *MNRAS*, 360, 533
- Davies, R. D. 1974, in *Galactic Radio Astronomy*, eds. F. J. Kerr, & S. C. Simonson, 60, 275
- De Buizer, J. M. 2006, *ApJ*, 642, L57
- Deguchi, S., & Watson, W. D. 1989, *ApJ*, 340, L17
- Ellingsen, S. P., Voronkov, M. A., Cragg, D. M., et al. 2007, in *Astrophysical Masers and their Environments*, eds. J. M. Chapman, & W. A. Baan, 242, 213
- Gray, M. D., Field, D., & Doel, R. C. 1992, *A&A*, 262, 555
- Green, J. A., & McClure-Griffiths, N. M. 2011, *MNRAS*, 417, 2500
- Guillet, V., Jones, A. P., Forêts, Pineau Des, & G., 2009, *A&A*, 497, 145
- Hirota, T., Tsuboi, M., Fujisawa, K., et al. 2011, *ApJ*, 739, L59
- Hirota, T., Tsuboi, M., Kurono, Y., et al. 2014, *PASJ*, 66, 106
- Hu, B., Menten, K. M., Wu, Y., et al. 2016, *ApJ*, 833, 18
- Hunter, T. R., Brogan, C. L., MacLeod, G., et al. 2017, *ApJ*, 837, L29
- Kurtz, S., Churchwell, E., & Wood, D. O. S. 1994, *ApJS*, 91, 659
- Lekht, E. E., Pashchenko, M. I., Rudnitskij, G. M., & Tolmachev, A. M. 2018, *Astron. Rep.*, 62, 213
- Liljeström, T., & Gwinn, C. R. 2000, *ApJ*, 534, 781
- MacLeod, G. C., Sugiyama, K., Hunter, T. R., et al. 2019, *MNRAS*, 489, 3981
- Molinari, S., Brand, J., Cesaroni, R., & Palla, F. 1996, *A&A*, 308, 573
- Moscadelli, L., Sanna, A., Goddi, C., et al. 2020, *A&A*, 635, A118
- Navarete, F., Damineli, A., Barbosa, C. L., & Blum, R. D. 2015, *MNRAS*, 450, 4364
- Reid, M. J., Menten, K. M., Brunthaler, A., et al. 2014, *ApJ*, 783, 130
- Sánchez-Monge, Á., López-Sepulcre, A., Cesaroni, R., et al. 2013, *A&A*, 557, A94
- Sanna, A., Surcis, G., Moscadelli, L., et al. 2015, *A&A*, 583, L3
- Shepherd, D. S., & Churchwell, E. 1996, *ApJ*, 457, 267
- Shimoikura, T., Kobayashi, H., Omodaka, T., et al. 2005, *ApJ*, 634, 459
- Sobolev, A. M., Bisyarina, A. P., Tatarsnikov, A. M., Antokhin, I., & Volvach, A. E. 2017, *ATel*, 10788, 1
- Sobolev, A. M., Moran, J. M., Gray, M. D., et al. 2018, *ApJ*, 856, 60
- Sobolev, A. M., Bisyarina, A. P., Gorda, S. Y., & Tatarsnikov, A. M. 2019, *Res. Astron. Astrophys.*, 19, 038
- Stecklum, B., & Caratti o Garatti, A., Klose, S., & Wiseman, P., 2017, *ATel*, 10842, 1
- Sugiyama, K., Saito, Y., Akitaya, H., Yonekura, Y., & Momose, M. 2017, *ATel*, 10757, 1
- Sugiyama, K., Saito, Y., Yonekura, Y., & Momose, M. 2019, *ATel*, 12446, 1
- Sunada, K., Nakazato, T., Ikeda, N., et al. 2007, *PASJ*, 59, 1185
- Todd, S. P., & Ramsay Howat, S. K. 2006, *MNRAS*, 367, 238
- Volvach, A. E., Volvach, L. N., MacLeod, G., et al. 2017a, *ATel*, 10853, 1
- Volvach, A. E., Volvach, L. N., MacLeod, G., et al. 2017b, *ATel*, 10728, 1
- Zavagno, A., Deharveng, L., Nadeau, D., & Caplan, J. 2002, *A&A*, 394, 225